

# The extremely low-luminosity Type Iax SNe 2022ywf and 2023zgx

B. Barna<sup>1,2</sup>, D. Bánhidi<sup>1</sup>, T. Szalai<sup>1,3</sup>, J. P. Anderson<sup>4</sup>, T. Boland<sup>5,6</sup>, K. A. Bostroem<sup>7,8</sup>, T.-W. Chen<sup>9</sup>, J. Farah<sup>10,11</sup>, M. Gromadzki<sup>12</sup>, G. Hosseinzadeh<sup>13</sup>, D. A. Howell<sup>10,11</sup>, C. Inserra<sup>14</sup>, S. W. Jha<sup>5</sup>, L. Kwok<sup>15</sup>, C. Macrie<sup>5</sup>, C. McCully<sup>10,11</sup>, E. Mochnács<sup>1</sup>, T. E. Müller-Bravo<sup>16,17</sup>, M. Newsome<sup>18</sup>, E. Padilla Gonzalez<sup>10,11</sup>, J. Pearson<sup>7</sup>, T. Petrushevska<sup>19</sup>, D. J. Sand<sup>7</sup>, M. Shrestha<sup>20,21</sup>, N. Smith<sup>7</sup>, S. Srivastav<sup>22</sup>, G. Terreran<sup>10,11</sup>, and J. Vinkó<sup>1,23</sup>

- <sup>1</sup> Department of Experimental Physics, University of Szeged, Dóm tér 9, H-6720 Szeged, Hungary
- <sup>2</sup> HUN-REN-SZTE Stellar Astrophysics Research Group, 6500 Baja, Szegedi út, Kt. 766, Hungary
- <sup>3</sup> MTA-ELTE Lendület "Momentum" Milky Way Research Group, Szent Imre H. st. 112, 9700 Szombathely, Hungary
- <sup>4</sup> European Southern Observatory, Alonso de Córdova 3107, Vitacura, Casilla 19001, Santiago, Chile
- <sup>5</sup> Department of Physics and Astronomy, Rutgers, the State University of New Jersey, 136 Frelinghuysen Road, Piscataway, NJ 08854, USA
- <sup>6</sup> Department of Physics and Astronomy, Purdue University, 525 Northwestern Ave, West Lafayette, IN 47907, USA
- <sup>7</sup> Steward Observatory, University of Arizona, 933 North Cherry Avenue, Tucson, AZ 85721-0065, USA
- <sup>8</sup> LSST-DA Catalyst Fellow
- <sup>9</sup> Graduate Institute of Astronomy, National Central University, 300 Jhongda Road, 32001 Jhongli, Taiwan
- <sup>10</sup> Las Cumbres Observatory, 6740 Cortona Drive, Suite 102, Goleta, CA 93117-5575, USA
- <sup>11</sup> Department of Physics, University of California, Santa Barbara, CA 93106-9530, USA
- <sup>12</sup> Astronomical Observatory, University of Warsaw, Al. Ujazdowskie 4, 00-478 Warszawa, Poland
- <sup>13</sup> Department of Astronomy & Astrophysics, University of California, San Diego, 9500 Gilman Drive, MC 0424, La Jolla, CA 92093-0424, USA
- <sup>14</sup> Cardiff Hub for Astrophysics Research and Technology, School of Physics & Astronomy, Cardiff University, Queens Buildings, The Parade, Cardiff, CF24 3AA, UK
- <sup>15</sup> Center for Interdisciplinary Exploration and Research in Astrophysics (CIERA), 1800 Sherman Ave., Evanston, IL 60201, USA
- <sup>16</sup> School of Physics, Trinity College Dublin, The University of Dublin, Dublin 2, Ireland
- <sup>17</sup> Instituto de Ciencias Exactas y Naturales (ICEN), Universidad Arturo Prat, Chile
- <sup>18</sup> Department of Astronomy, The University of Texas at Austin, 2515 Speedway, Stop C1400, Austin, TX 78712, USA
- <sup>19</sup> Center for Astrophysics and Cosmology, University of Nova Gorica, Vipavska 11c, 5270 Ajdovščina, Slovenia
- <sup>20</sup> School of Physics and Astronomy, Monash University, Clayton, Australia
- <sup>21</sup> OzGrav: The ARC Center of Excellence for Gravitational Wave Discovery, Australia
- <sup>22</sup> Astrophysics sub-Department, Department of Physics, University of Oxford, Keble Road, Oxford, OX1 3RH, UK
- <sup>23</sup> Konkoly Observatory, Research Centre for Astronomy and Earth Sciences, Konkoly Thege Miklós út 15-17, H-1121 Budapest, Hungary

February 27, 2026

## ABSTRACT

**Context.** We present the optical follow-up of SNe 2022ywf and 2023zgx, two examples from the Iax subclass of thermonuclear supernova (SN) events. With peak absolute magnitudes of  $M_V = -13.7$  and  $-14.4$  mag, respectively, both objects belong to the extremely low-luminosity (EL) population of the class.

**Aims.** A common origin of SNe in the Iax subclass is still under debate since the distribution of certain observables may indicate that the extremely low-luminosity explosions form a distinct population. We aim to estimate the physical properties of the two EL objects, including mapping the ejecta structure. The results are compared to the predictions of the pure deflagration model with similar luminosity, as well as the common features of other SNe Iax.

**Methods.** We perform spectral tomography on the spectral series of SNe 2022ywf and 2023zgx around their maxima to map the physical properties of the ejecta. Together with the analysis of *BgVriz* photometry, a wide range of observables can be studied to investigate their distribution against luminosity. The constrained chemical abundances of the ejecta are compared to the predictions of the hydrodynamic simulations with similar peak luminosities.

**Results.** Constant abundances provide a good match for the distribution of chemical elements for both SNe 2022ywf and 2023zgx. The discrepancies compared to the least luminous pure deflagration model *N5def\_hybrid* are minor, especially at post-maximum epochs. The two SNe also share similar characteristics in their constrained density structures, as well as the evolution of the photosphere.

**Conclusions.** The analysis supports the assumption that pure deflagration models can reproduce the main characteristics of SNe Iax, even for the low-luminosity population. The presented indirect observational evidence indicates that these objects show similar intrinsic properties to the well-studied, relatively luminous Iax sample and fit into the velocity distribution of the subclass.

**Key words.** supernovae: individual: SNe 2022ywf; supernovae: Type Iax supernovae; radiative transfer; spectral tomography;

## 1. Introduction

SNe Ia originate from the thermonuclear explosion of C/O white dwarfs (WDs). Although significant exploration has still not confirmed the most probable progenitor and explosion scenario, the remarkable homogeneity of the so-called ‘normal’ SNe Ia makes the Ia class the most important objects for distance estimations Phillips (1993). However, the several subclasses of thermonuclear SNe (Taubenberger 2017) indicate that there are multiple channels for degenerate WDs; thus, studying these peculiar explosions provides essential information on SN physics.

The most numerous subclass of thermonuclear SNe Ia is formed by the Iax (or, after their prototype object, ‘2002cx-like’) SNe. The volume-limited samples of nearby surveys investigated by Foley et al. (2013) indicate a  $31^{+17}_{-13}\%$  relative rate of SNe Iax to normal Ia explosions. However, the sample from the recent Data Release 2 of the Zwicky Transient Facility (which included  $\sim 3600$  and  $\sim 1580$  thermonuclear SNe in the total and volume-limited samples, respectively) indicates that the relative rate of SNe Iax reached only  $\sim 4.5\%$  Dimitriadis et al. (2025). A possible reason for the discrepancy is that the relative rates of sub-luminous SNe Ia can be estimated only by assuming correction factors for the lower probability of detection and classification. This can be critical for SNe Iax with the lowest peak luminosity and shorter light curve widths, adding high uncertainty for population estimates.

The lower peak luminosity of SNe Iax also strongly limits the sample suitable for detailed analysis, in contrast to the normal SNe Ia. Since the first classification (SN 2002cx, Li et al. 2003), approximately 110 transients have been identified as type Iax SN according to WISEREP<sup>1</sup>, but there are fewer than 20 of them with published well-sampled photometric and spectroscopic datasets. The extreme diversity of the subclass hinders the investigation of the nature of type Iax SNe. Their peak absolute magnitude covers a wide range, from the relatively luminous objects with a peak absolute magnitude of  $M_R = -18.60$  mag (SN 2011ay, Szalai et al. 2015) to extremely faint ones with  $M_r = -12.66$  mag (SN 2019gsc, Karambelkar et al. 2021) in the R/r-band. Similarly, other physical characteristics of these SNe also show extremities, such as the decline rate, spectral velocities, or implied ejecta masses.

Multiple mechanisms have been assumed to explain the peculiar nature of Iax explosions. So far, the pure (or, as it is often called, “failed”) deflagration scenario has been considered the most promising concept (for a full review, see Lach et al. 2022). Hydrodynamic simulations (Jordan et al. 2012; Kromer et al. 2013; Long et al. 2014; Fink et al. 2014; Kromer et al. 2015; Leung & Nomoto 2020; Lach et al. 2022) have shown that the diverse physical properties of the sample can be reproduced by scaling the strength of the deflagration of a C/O WD. A common feature in all pure deflagration models is that the kinetic energy is not sufficient to fully unbind the WD; thus, the explosion leaves behind a bound remnant. As a further consequence, the ejecta of a SN Iax is expected to have a lower mass and a lower average density than that of normal SNe Ia. However, this scenario cannot account for the least luminous SNe Iax, represented by the prototype SN 2008ha. For this object, a C/O/Ne WD was proposed as a potential progenitor, which successfully decreased the produced energy - and, thus, also the luminosity - of the models (Kromer et al. 2015). Note that no other pure deflagration model has produced SNe fainter than  $M_r > -15$  mag, while Kromer et al. (2015) presented the hydrodynamic simulation of only one scenario. Since SN 2008ha, even less luminous

SNe have been discovered (e.g. SNe 2019gsc, 2021fcg, 2024vjm Tomasella et al. 2020; Srivastav et al. 2020; Karambelkar et al. 2021; Kwok et al. 2025). For these objects, the double degenerate merger model presented by Kashyap et al. (2018) can reproduce their peak absolute magnitudes and low ejected masses. This scenario results in a failed detonation, providing numerous testable discrepancies compared to the concept of failed deflagration, such as the strong stratification of chemical elements or the relatively higher expansion velocities.

A major breakthrough in understanding SNe Iax came with the discovery of the progenitor system of SN 2012Z (McCully et al. 2014; Stritzinger et al. 2015) in pre-explosion HST images of its host NGC 1309. The luminous blue progenitor makes it highly probable that the system included a helium-star donor and an accreting near-Chandrasekhar mass WD. If this interpretation is correct, it directly confirms that at least some WD SNe come from the single degenerate scenario (McCully et al. 2014). In contrast, no luminous companion star has ever been directly observed for a normal SN Ia, or any other SNe Iax.

Therefore, the common origin of the extremities of SNe Iax is still under debate, and most studies divide the subclass into luminosity samples. Srivastav et al. (2022a) draw the line at peak absolute magnitude  $M_V = -16$  mag to distinguish the “faint” SNe Iax from the rest of the category. Singh et al. (2023) argued for the existence of clustering among SNe Iax, as the “faint” ( $M_r > -14.6$  mag) and “bright” ( $M_r < -17.1$  mag) samples showed different correlations between peak luminosity and the  $\Delta m_{15}$  parameter describing the fading after the peak. SNe Iax with an intermediate luminosity range between the two groups presented by Singh et al. (2023) have long been known; however, their low numbers and the lack of observational series have made their characterization difficult. The first example with a detailed analysis, SN 2019muj (Barna et al. 2021), showed a transitional nature that bridged the luminosity gap between the faint and bright groups. The constrained intrinsic characteristics (e.g., ejecta mass, expansion velocities) and the spectroscopic evolution imply that most of the physical properties and observables change continuously through the entire Iax subclass, instead of clustering. Recent studies of objects with similar luminosities (SNe 2022xlp and 2024pxl, Bánhidi et al. 2025; Singh et al. 2025, respectively) also supported this result. Whether or not there are differences in their origin scenarios, labeling various groups of the diverse Iax subclass is useful for referencing the objects with different properties. We suggest, and hereafter use, a three-level (sub-)classification:

- Relatively luminous (RL) group: ( $M_r < -17$  mag), example: SN 2011ay
- Intermediate luminous (IL) group: ( $-14.5$  mag  $> M_r > -17$  mag), example: SN 2019muj
- Extremely-low luminosity (EL) group: ( $M_r > -14.5$  mag), example: SN 2008ha

As discussed above, the diverse nature of SNe Iax can be fully understood only by sampling the entire subclass. The cases of SNe 2022ywf and 2023zgx, both peaking around  $M_V \sim -14$  mag, are presented in this study to provide further characteristics in observables and physical properties, particularly of the lowest-luminosity events of this class. The paper is organized as follows. In Sec. 2 we describe the discovery of the two objects and the properties of their host galaxies, followed by the sources and the properties of the observed datasets. We introduce the techniques used to analyze the photometric and spectroscopic data in Secs. 3 and 4, respectively, and describe the inferred results. The conclusions are summarized in Sec. 5.

<sup>1</sup> WISEREP can be accessed at <https://www.wiserep.org/>

## 2. Observations

### 2.1. SN 2022ywf

SN 2022ywf (RA 01:22:12.20, DEC +00:57:23.55) was discovered by the Zwicky Transient Facility (ZTF) at 59880.18 MJD while still on the rise at  $m_r = 19.95$  mag with the last non-detection from 59879.33 MJD with a magnitude limit of 20.4 mag in g-band. The field of SN 2022ywf was also observed by the Asteroid Terrestrial-impact Last Alert System program (ATLAS; Tonry et al. 2018), providing a deep, 20.7 mag non-detection limit in cyan-band on 59879.19 MJD. Classification as type Ia SN was based on the first spectrum obtained at 59881.3 MJD (Bostroem et al. 2022), which was then refined to be a type Iax with subsequent data (Srivastav et al. 2022b). The host of SN 2022ywf is NGC 493, an SBc type galaxy. The distance of NGC 493 has been constrained multiple times by following the Tully-Fisher relation. These results converged to the range of 22.0–24.5 Mpc in the past decade. Hereafter, we use the latest  $d = 22.8 \pm 4.7$  Mpc distance estimation of (Tully et al. 2016). The SN appeared at 50" ( $\sim 5600$  pc) north-east from the center of the host galaxy. Due to its relatively outskirts location in the galactic disk, and because of the non-detection of the Na I D lines at the redshift of NGC 493, we can safely assume negligible host-galaxy reddening.

The ATLAS photometry at the position of SN 2022ywf was obtained through the public forced photometry server<sup>2</sup> (Shingles et al. 2021). In addition to the measured fluxes (in microjansky or  $\mu$  Jy) and associated errors, the forced photometry server also returns quality metrics including a reduced chi squared for the point spread function (PSF) fitting (labeled  $\chi/N$ ). Individual measurements with an error exceeding  $150 \mu$ Jy were rejected, along with measurements with  $\chi/N > 3$ . ATLAS typically obtains  $4 \times 30$  s exposures spaced within  $\sim 1$  hr. Each quad of individual measurements that passed the quality cuts defined above were combined into a single measurement using a weighted stacking recipe following Srivastav et al. (2023). Stacked measurements with  $3\sigma$  significance were considered as detections, and an AB magnitude was derived using  $m_{AB} = -2.5 \times \log(F_{\mu\text{Jy}}^{\text{stack}}) + 23.9$ . The non-detections were converted into  $3\sigma$  upper limits using  $m_{AB} > -2.5 \times \log(3 \times \Delta F_{\mu\text{Jy}}^{\text{stack}}) + 23.9$ .

The Las Cumbres Observatory (LCO) initiated follow-up at 59880.8 MJD, providing *BgVri* light curves obtained with multiple 1-m telescopes (Brown et al. 2013) located at Sutherland (South Africa), CTIO (Chile), Siding Spring (Australia), and McDonald (USA) observatories, through the Global Supernova Project (GSP). After +30 days, *BV* light curves showed highly scattered and uncertain magnitudes, but the *gri* data are included until 59984 MJD, when the photometric monitoring ceased (Tab. A.3). The ATLAS survey followed SN 2022ywf in *c*- and *o*-bands. The first detection was at 59880.45 MJD ( $m_c = 19.60 \pm 0.14$  mag) and it was regularly observed until 59931.6 MJD, when the target faded below the detection limit (Tab. A.1). The light curves of SN 2022ywf obtained in ATLAS *o*- and *c*-bands are shown in Fig. 1, while the *BgVri* photometry of SN 2022ywf is compared to that of SN 2023zgx in Fig. 2.

Optical spectroscopy of SN 2022ywf was obtained by the 9.2-m Southern African Large Telescope (SALT) with the Robert Stobie Spectrograph (RSS) through the Rutgers University program. LCO optical spectra were taken with the FLOYDS spectrographs mounted on the 2-m Faulkes Telescope North and South at Haleakala (USA) and Siding Spring (Australia) through

the GSP. Three spectral epochs were observed with the Low Resolution Spectrograph 2 (LRS2) (Chonis et al. 2014) mounted on the Hobby-Eberly Telescope (HET, Ramsey et al. 1998) located at McDonald Observatory. Two spectra were obtained with the Southern Astrophysical Research (SOAR) Telescope using the red camera of the Goodman High-Throughput Spectrograph (GHTS; Clemens et al. 2004) and were reduced using the Goodman Pipeline.<sup>3</sup> Additional spectra were observed with the KOSMOS medium resolution spectrograph equipped on the Apache Point Observatory (APO) ARC 3.5m Telescope (); with the Boller and Chivens Spectrograph (B&C) on the University of Arizona's Bok 2.3m telescope located at Kitt Peak Observatory; the ESO Faint Object Spectrograph and Camera version 2 (EFOSC2; Buzzoni et al. 1984) at the 3.6-m New Technology Telescope (NTT) in the frame of the ePESSTO+ collaboration (Smartt et al. 2015); and using the SPRAT low resolution spectrograph on the Liverpool Telescope (LT). All optical spectra of SN 2022ywf are shown in Fig. 3.

### 2.2. SN 2023zgx

SN 2023zgx (RA 12:44:05.00, DEC -05:40:53.47) was discovered by Koichi Itagaki at 60287.8 MJD, likely a few days before its peak, at a visual brightness of 16.9 mag. The classification spectrum, based on which the transient was characterized as a faint type Iax SN, was obtained only four days later (Crimes et al. 2023), and photometric follow-up started during its decline. SN 2023zgx was associated with the DDO 142 type S galaxy. The only distance estimate apart from the Hubble-flow gives  $25.4 \pm 5$  Mpc for the distance (Tully & Fisher 1988), which is used in this study. This distance is higher than that calculated from the redshift of 0.0047 ( $d_z = 20.2$  Mpc), but still consistent with it. SN 2023zgx was also monitored by the LCO sites, providing *BgVri* light curves between 60294.7 and 60378.2 MJD.

The first spectrum of SN 2023zgx was observed with the Gemini Multi-Object Spectrograph mounted at Gemini North (GMOS-N; Hook et al. 2004) two days before the start of the photometric monitoring. Spectroscopic follow-up was initiated by ePESSTO+ collaboration (Smartt et al. 2015) with the EFOSC2/NTT and GSP with multiple LCO/FLOYDS spectrographs. Late-time ( $t + 80$  days) spectra were obtained with SALT/RSS between +80 and +90 days after the r-band maximum.

The observed *BgVriz* photometry of SN 2023zgx can be found in Tab. A.5, while the reduced spectra, corrected for host-galaxy redshift, are shown in Fig. 4. For further analysis, all spectra were scaled to the photometry using a polynomial function and dereddened for Milky Way extinction.

## 3. Photometric analysis

For SN 2022ywf, the photometric coverage is suitable for fitting a low-order polynomial function to the LCs of each filter around the maximum, extending to +20 days. The inferred parameters, such as peak magnitude and  $\Delta m_{15}$  decline rate, are listed in Tab. 1. Considering the  $\mu = 31.79$  mag distance modulus and the MW reddening (assuming no host galaxy reddening based on the lack of Na I D lines) the peak absolute magnitude of SN 2022ywf is  $M_r = -13.81 \pm 0.44$  mag, placing the object in the EL group of the Iax subclass. Based on their peak luminosities, the closest relatives to SN 2022ywf are SNe 2008ha and 2019gsc. The polynomial fits provided  $T_{\text{max}} = 59890.4$  MJD) for the moment

<sup>2</sup> <https://fallingstar-data.com/forcedphot/>

<sup>3</sup> <https://soardocs.readthedocs.io/projects/goodman-pipeline/>

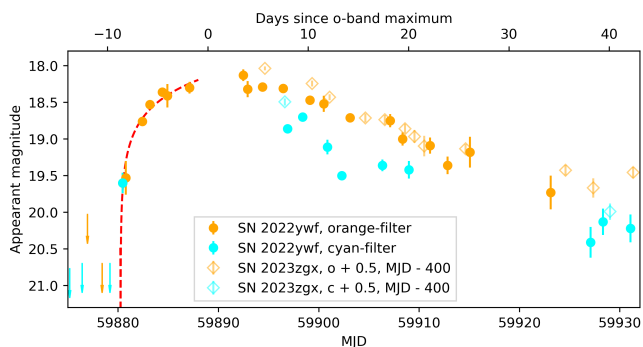


**Fig. 1.** ATLAS photometry of SNe 2022ywf and 2023zgx. The observation dates of SN 2023zgx are shifted with 400 days earlier. The red dashed line shows the fit of Eq. 1 on the pre-maximum *o*-band data of SN 2022ywf.

of maximum light in *r*-band, which is used as a further reference date, similarly to our previous works.

The ATLAS *co*-band LCs provide early detections supplemented with deep non-detection limits ( $> 20.7$  mag). The steeply rising early part of the SN LCs can be fitted with the so-called simple *fireball* model (Riess et al. 1999), where we assume a constant photospheric temperature ( $T_{\text{eff}}$ ) and velocity ( $v_{\text{phot}}$ ); thus, the emerged flux is a quadratic function of the time since the explosion ( $F \sim t_{\text{exp}}$ ). Firth et al. (2015) showed on a large sample of normal Ia SNe that these assumptions are not robust, and while the early rise of the LC can be fitted with a power-law function:

$$F = a \cdot (t - t_{\text{exp}})^n, \quad (1)$$

the  $n$  exponent, referred to as rise index, covers a wide range between 1.5 and 2.5 and has a mean value of  $n = 2.44$ . In the case of the subluminous Type Iax SNe, the fit of the rise index results in a typically lower value. Magee et al. (2025) recently studied the rising curves of all available SNe Iax with detailed pre-maximum coverage and found that rise indices of SNe Iax show a similar scattering to normal SNe Ia, but with a lower mean value of 1.4–1.5 in the *g*- and *r*-bands. Their sample was mainly limited to the RL group but also included the faintest type Iax SN 2024vjm ( $M_L = -13.19 \pm 0.15$  mag), for which a rise index of  $n_L = 0.94^{+0.32}_{-0.34}$  was measured. Similar analyzes of individual SNe showed that the least luminous objects (e.g. SNe 2015H, 2019muj and 2020udy, Magee et al. 2016; Barna et al. 2021; Singh et al. 2024, respectively) have rise indices  $n < 1.3$ , indicating that there might be a link between luminosity and the rising parameters of type Iax SNe.

Handling the rise index as a free parameter in the fitting of the SN 2022ywf *o*-band LC (see Fig. 1), which includes the most pre-maximum observations, would return an extremely low exponent ( $n = 0.38 \pm 0.09$ ) and might be an unrealistic first light date ( $T_0 = 59880.25 \pm 0.22$  MJD) coinciding with the time of the discovery (59880.17 MJD). This inconsistency is probably due to the effect of insufficient coverage of the rising phase, with six pre-maximum observations in *o*-band and even fewer with other filters. Thus, we assume the time of first light based on the last-non-detection and the first detection in *c*-band as  $T_0 = 59879.8 \pm 0.6$  MJD.

As an alternative way to estimate  $T_0$ , and thus the rise time, the abundance tomography analysis (see Sec. 4.1) also provides constraints on the time of first light, as the fit of the spectral time series includes the input parameter  $t_{\text{exp}}$  of the spectral fitting as

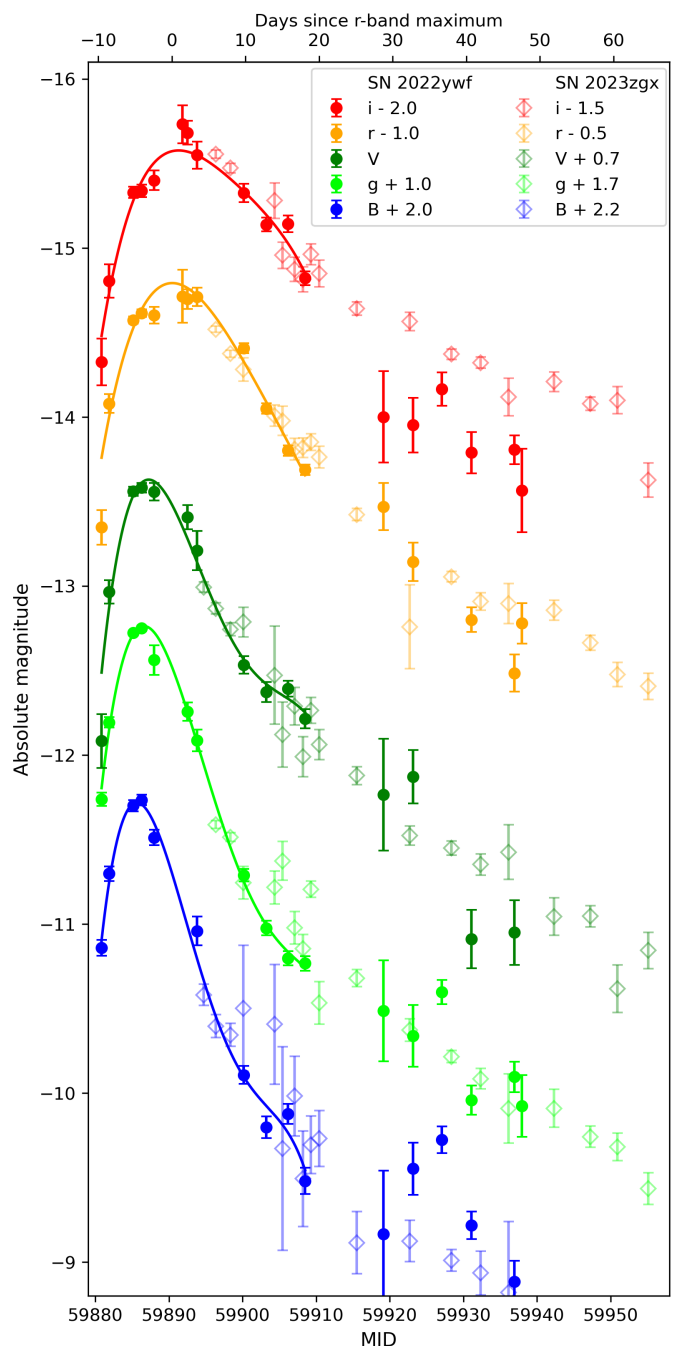


**Fig. 2.** Ground-based photometry of SNe 2022ywf (filled circles) and 2023zgx (fainter diamonds). The horizontal axis represents the observational dates of SN 2022ywf in MJD. For SN 2023zgx, the data points are shifted with 400 days earlier for better comparison. The LC fits with fourth-order polynomial functions are also shown for SN 2022ywf (solid lines).

the dilution factor of the density structure. However, the constrained densities mark the date of the explosion, which occurs earlier than the escape of the first photons from the ejecta, i.e., first light. The interim period, also called the dark phase, may cover a few days for SNe Ia (Piro & Nakar 2013) and explosion models with a compact  $^{56}\text{Ni}$  distribution (Magee et al. 2020). On the other hand, deflagration models predict dark phases shorter than one-day (Fink et al. 2014).

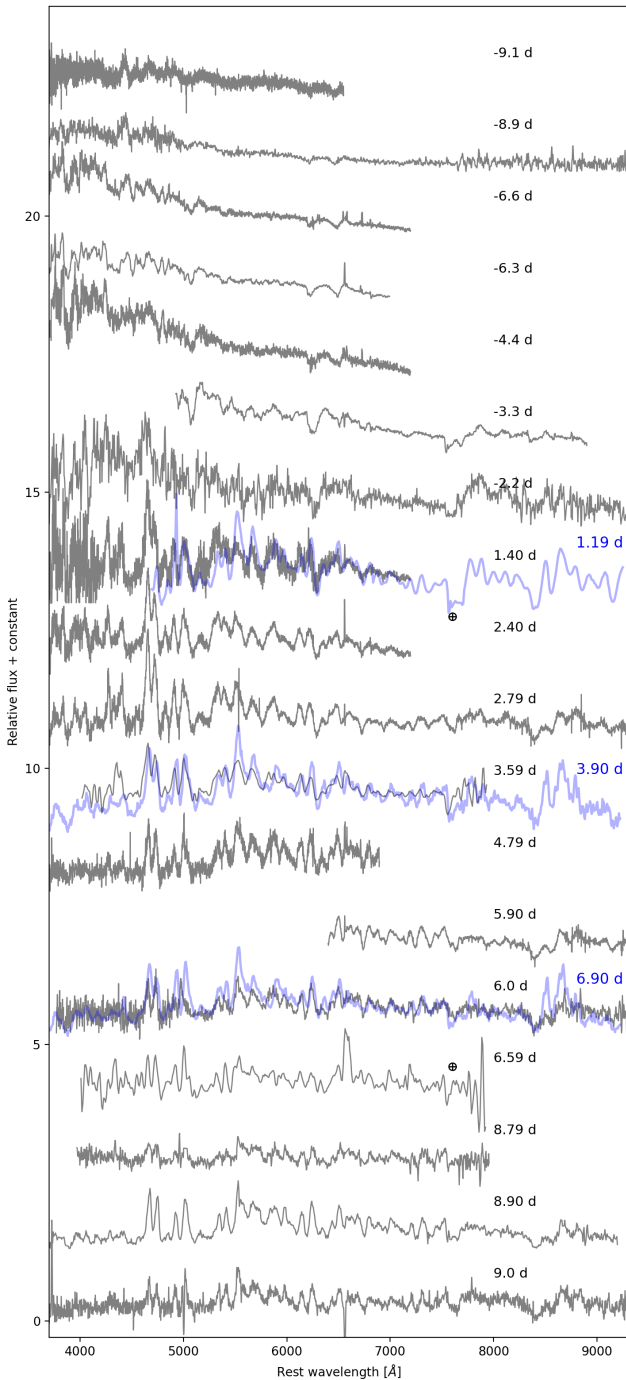


**Fig. 3.** Optical spectra of SN 2022ywf. The epochs show the days with respect to r-maximum. The observation log of spectra can be found in Tab. A.4. The first three spectra of SN 2023zgx (blue) close in phase to those of SN 2022ywf (grey) are also shown as comparison.

SN 2023zgx, the other subject of this study, peaks around -14.4 mag in *r*-band, based on the similarities with SN 2022ywf in post-maximum LCs and spectral evolution (see Fig. 2), but the same set of photometric parameters cannot be precisely estimated due to the lack of coverage of the pre-maximum data. However, the many similarities between the two SNe suggest that we can safely assume a similar light curve evolution and constrain the time of peak brightness of SN 2023zgx based on that of SN 2022ywf. The declining LCs in *g*-, *V*- and *r*-bands

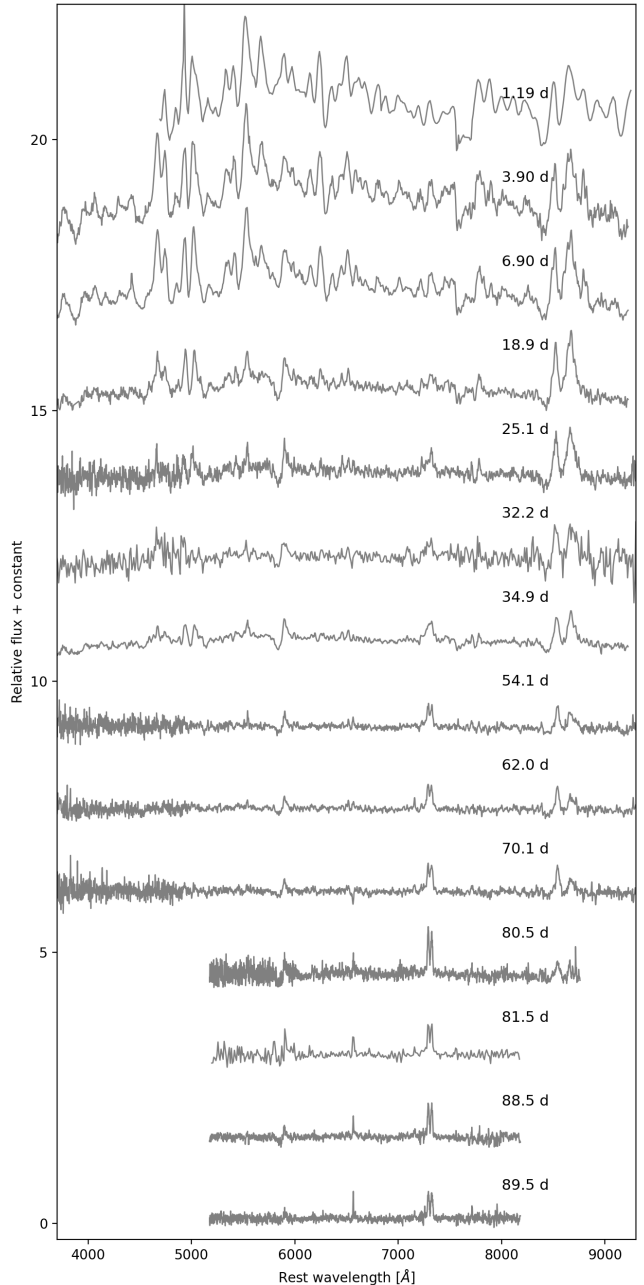


**Fig. 4.** Optical spectra of SN 2023zgx. The epochs show the days with respect to r-maximum. The observation log of spectra can be found in Tab. A.6.

can be overlapped with those of SN 2022ywf in the first two weeks after maximum by assuming a shift of  $\Delta t = T_{23zgx}(r_{\max}) - T_{22ywf}(r_{\max}) = 400$  days along the time-axis (see Fig. 2) and  $\Delta m_r = +0.2$  mag along the magnitude-axis. Assuming the same  $\Delta t$  provides an excellent match with the ATLAS *c*- and *o*-band light curves of the two SNe with a slightly greater shift in brightness ( $\Delta m_o = 0.5$  mag). Assuming the presented match with the shifted LCs, we consider  $T_{23zgx}(r_{\max}) = 60290.4$  MJD as a rough estimate of the date of maximum, which is used as the reference time for epochs of SN 2023zgx hereafter, with an approximate uncertainty of  $\pm 3$  days. The comparison of LCs may indicate that SN 2023zgx fades more slowly; however, it is important to note that this statement is mainly supported by the photometry after +20 days, when observations of SN 2022ywf become un-

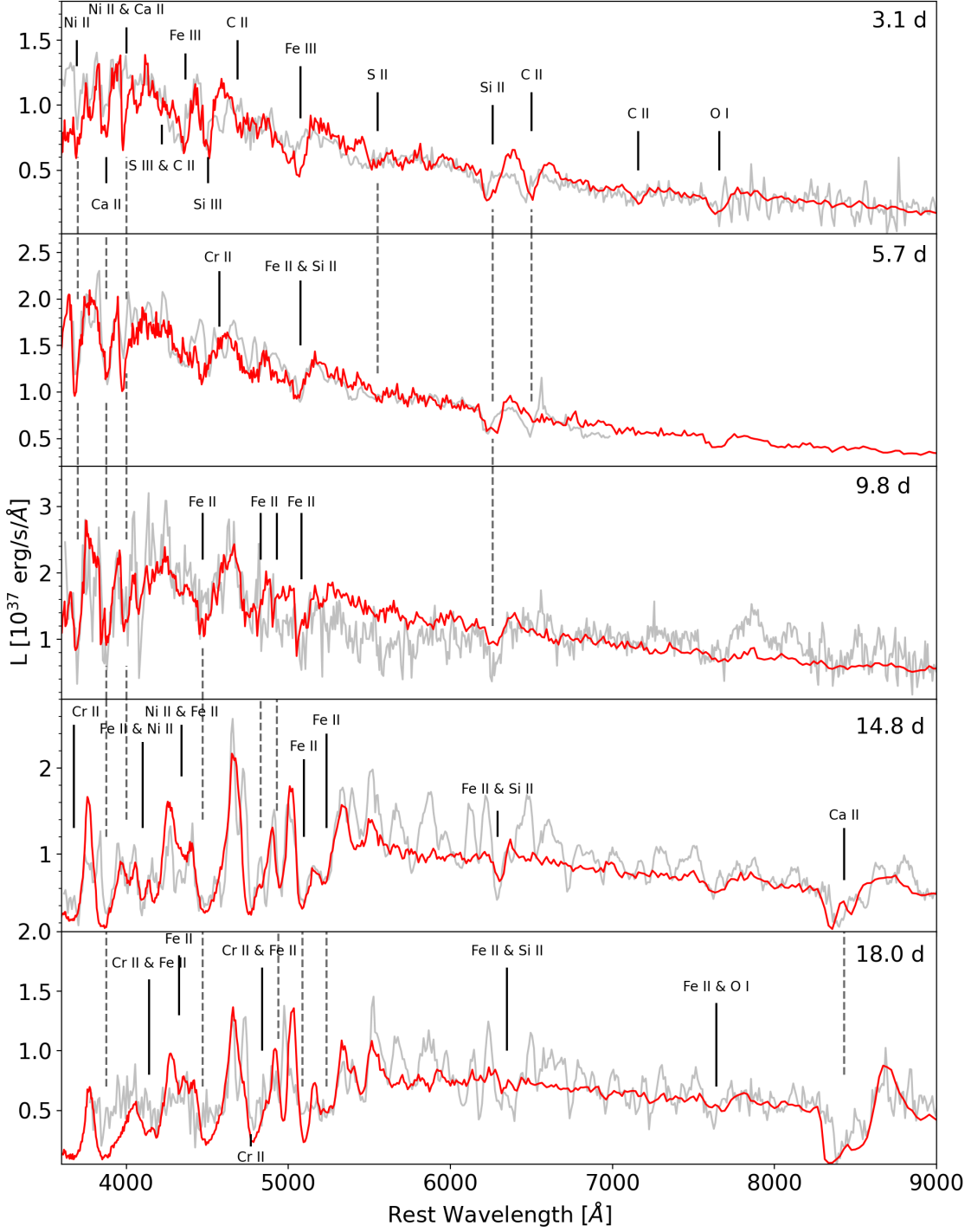


**Fig. 5.** Five spectral epochs of SN 2022ywf (grey) fitted with the TARDIS synthetic spectra (red) produced in the abundance tomography analysis.

certain. The decline rates show significant differences in the B- and i-filters, which suggest different color evolutions for the two objects. The lack of pre-maximum photometry of SN 2023zgx limits the determination of the date of explosion. Quantitative estimates of  $T_{\text{exp}}$  are constrained by the abundance tomography analysis described in Sec. 4.

#### 4. Spectral analysis

The optical spectra of SNe 2022ywf and 2023zgx are shown in Figs 3 and 4, respectively. Due to the short sampling period of SN 2022ywf and the lack of pre-maximum epochs of SN 2023zgx, there is only a short period of a few days when the two spectral series overlap in phases. The three spectra of SN 2023zgx during this period show excellent matches with those of SN 2022ywf, which underlines the general similarity of the intrinsic properties of the two objects. SN 2022ywf evolves

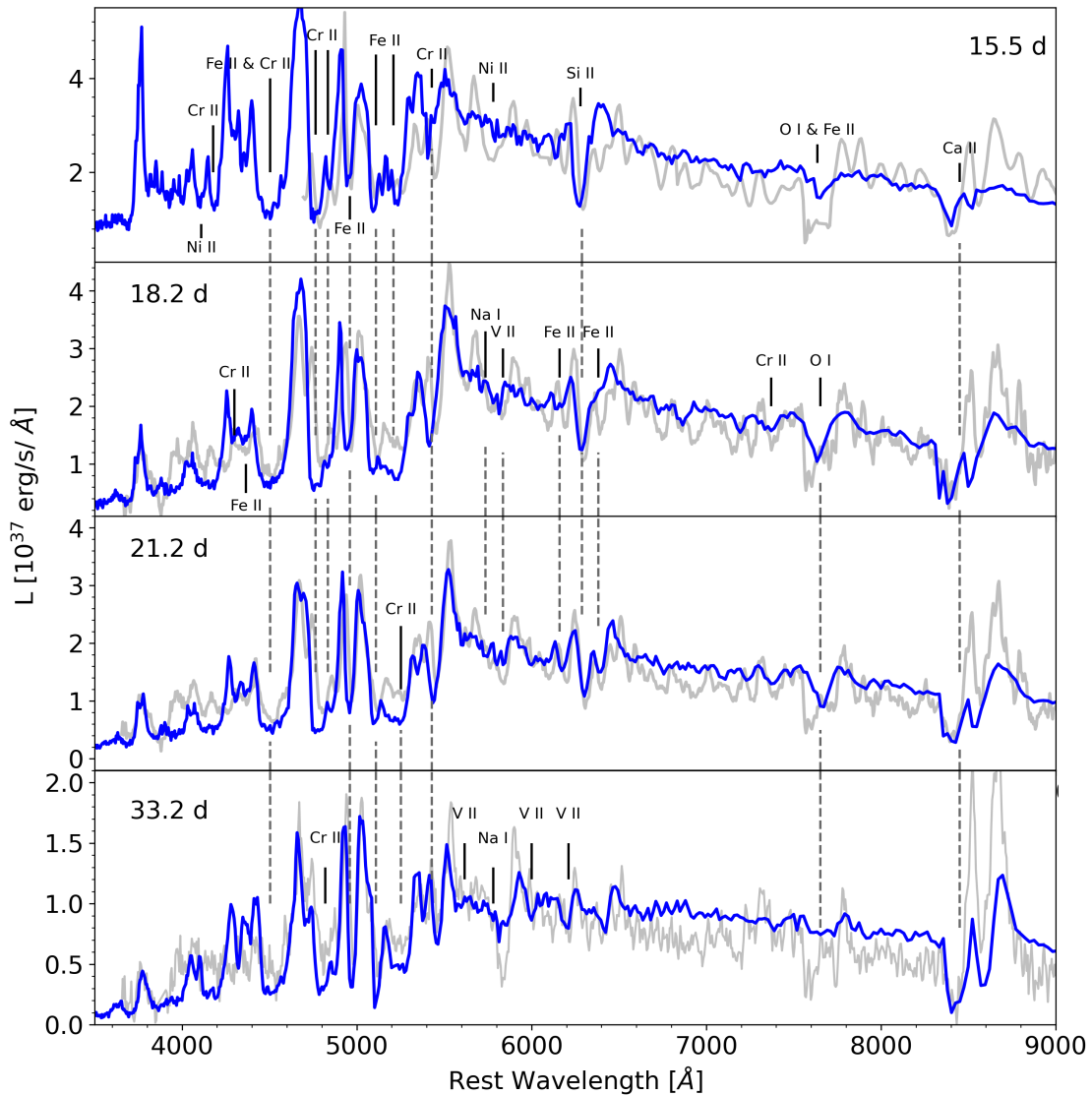


**Fig. 6.** Four spectral epochs of SN 2023zgx (grey) fitted with the TARDIS synthetic spectra (blue) produced in the abundance tomography analysis.

**Table 1.** The light curve parameters of SN 2022ywf.

	B	g	V	r	i
$T_{\max}$ [MJD]	59885.6 (0.16)	59886.6 (0.1)	59687.2 (0.2)	59890.4 (0.3)	59891.3 (0.6)
$m$ [mag]	18.18 (0.02)	18.12 (0.02)	18.25 (0.02)	18.06 (0.02)	18.25 (0.04)
$M$ [mag]	-13.74 (0.44)	-13.77 (0.44)	-13.68 (0.44)	-13.81 (0.44)	-13.59 (0.44)
$\Delta m_{15}$ [mag]	1.65 (0.03)	1.67 (0.03)	1.19 (0.03)	0.91 (0.04)	0.58 (0.10)
$t_{\text{rise}}$ [days]	5.6 (1.5)	6.6 (1.6)	7.6 (1.5)	10.4 (1.6)	11.3 (2.0)

slightly faster, as can be seen in the shifting epochs of the matching spectra. This might be the result of the shorter diffusion timescale due to the lower ejecta mass, which can be tested by comparing the inferred density profiles from abundance tomography (see below).

We analyze the first 20 days of the spectral time series of SNe 2022ywf and 2023zgx sampled with seven and four spectra, respectively, obtained at pre- and near-maximum epochs. In this period, the assumptions of TARDIS (Kerzendorf & Sim 2014), such as the existence of a sharp photosphere, are rather robust, allowing for the rapid modeling of realistic synthetic spectra for the optical regime. We aim to fit these spectral time series listed

in Tabs. A.4 and A.6 follow the method of abundance tomography analysis. This technique assumes that line formation occurs mainly close to the photosphere; thus, each spectral epoch can constrain a certain layer of the ejecta. The retreating photosphere allows for mapping the ejecta inward by fitting the spectral time series accordingly. The later epochs may indicate a review of the outer layers as well, since some chemical elements could form lines in a more diluted but cooler region of the ejecta.

Abundance tomography of SNe Iax has been performed in multiple studies since the first adaptations (Magee et al. 2016; Barna et al. 2017) of the TARDIS radiative transfer code (Kerzendorf & Sim 2014). The rapid evolution of the optical

spectra, together with the numerous unblended spectral features that, compared to those of normal SNe Ia, are not saturated, provides suitable cases for fitting a large number of parameters of the ejecta through rapid modeling with a simplified radiative transfer code. SNe 2002cx, 2005hk, 2012Z (Barna et al. 2018), 2019gsc (Srivastav et al. 2020), 2019muj (Barna et al. 2021), 2018cni, 2020kyg, (Singh et al. 2023) 2020udy (Singh et al. 2024) have been the subjects of similar abundance tomography, where the density profiles, abundance ratios, photospheric properties, and the times of explosions were constrained (the exact fitting strategy varies in each study; for further details, see the references). It is important to note that none of these modeling attempts aimed to find the best fit due to the large number of fitting parameters. Instead, our fitting process provides only a feasible solution for the model atmosphere (labeled as "best-fit" for simplicity) by testing and modifying the results of the *N5def\_hybrid* (Kromer et al. 2015) pure deflagration model.

#### 4.1. SN 2022ywf

As a first approach, we reduce the number of free parameters by adopting constant abundances based on the predictions of a corresponding deflagration model, similar to the analysis of SN 2014dt described by Camacho-Neves et al. (2023). Taking the peak luminosities, the only hydrodynamic simulation with  $M_V \sim 14$  mag is *N5def\_hybrid*, assuming the failed deflagration of a CONe-hybrid WD. The estimated observables of the hydro model showed a good match with the early photometric and spectroscopic evolution of the EL-Iax SN 2008ha, but it failed to reproduce the decline rate and the continuum flux weeks after the maximum. The adopted constant chemical composition based on the *N5def\_hybrid* (see Fig. 8) is characterized by C, O,  $^{56}\text{Ni}$ , and stable IGE (mostly Fe) as the most abundant elements, each having mass fractions of around 20%. While adopting this uniform chemical structure, we aim to fit the continuum and the line widths at each epoch, allowing us to constrain  $\rho(v)$ ,  $t_{\text{exp}}$  and  $v_{\text{phot}}$ , whose parameters affect the local temperature of the ejecta at first approximation.

For the density structure, we adopt a purely exponential function similar to that of *N5def\_hybrid*:

$$\rho(v, t_{\text{exp}}) = \rho_0 \cdot \exp^{-\frac{v}{v_0}} \cdot \left(\frac{t_{\text{exp}}}{t_0}\right)^{-3} \quad (2)$$

where  $\rho_0$  is the central density at  $t_0$  reference time (typically chosen as  $t_{\text{exp}} = 100$  s, the approximate end of the fusion processes and the beginning of homologous expansion). The  $v_0$  parameter characterizes the slope of the density profile. This model does not exhibit any cut-off in the outer layers, such as the similarly constrained density profiles of RL SNe (Barna et al. 2018) and the corresponding hydrodynamic models (Fink et al. 2014). Since the studied spectral series does not cover the vast majority of the ejecta, we cannot constrain the  $M_{\text{ej}}$  ejecta mass from abundance tomography; only the bolometric light curve fitting can provide an estimate of the ejecta mass. However, the fitted parameters of Eq. 2 allow a quantitative comparison between the outer layers of other SNe Iax and deflagration models.

The fit of the density structure is relatively uncertain, as the two main properties defining the function, the  $\rho_0$  central density parameter and the  $v_0$  slope of the exponential function, are strongly coupled. The segment of the density function sampled by a certain spectral epoch mainly affects the optical depth of the lines, but it also influences the temperature profile of the ejecta,

allowing us to constrain the densities. During the fitting process, we observed that TARDIS modeling is sensitive to changes in densities of at least 50% as it caused discrepancies in the observed spectral features that could not be compensated for by modifying chemical abundances or other physical parameters. The density function used for the SN 2022ywf model (see in Fig. 7).

Compared to the other two fitting parameters in the density function, the date of the explosion can be fitted precisely since it affects the entire spectral time series via the dilution of the density profile (see  $t_{\text{exp}}$  in Eq. 2). The best-fit value is found to be  $T_{\text{exp}} = 59878.4$  MJD. The early epochs, especially the first three between  $t_{\text{exp}} = 3.1$  and 5.7 days, are very sensitive to the  $T_{\text{exp}}$  parameter, as even a few hours can strongly modify the temperature profile and, thus, the continuum. Even though our method is not suitable for detailed uncertainty analysis, the estimated upper limit of the error of  $T_{\text{exp}}$  is  $\pm 0.5$  day. This provides a dark phase between the first light and the explosion as  $T_0 - T_{\text{exp}} = 1.4$  days.

As a second step, we continue the spectral fitting by allowing the constant mass fractions of elements that have a significant impact on the spectral features, namely C, Mg, Si, S, Ca, Fe, and the most abundant radioactive isotope,  $^{56}\text{Ni}$ , to vary. Note that TARDIS uses the actual state of decay products at each epoch, thus, abundances of Co and Fe increase with time. Other elements and isotopes, such as Ne, although relatively abundant ( $X(\text{Ne}) \simeq 0.03$ ), have a limited impact on the early optical evolution, and we keep their initial mass fraction fixed. Oxygen is used as a buffer element to manage the normalization of the total mass fraction of chemical elements to 1. Furthermore, the features of post-maximum epochs indicate the inclusion of Cr and V, two elements that may originate from the radioactive decay of  $^{54}\text{Fe}$  but are expected to be present in low abundances. The required mass fractions ( $X(\text{Cr}) \simeq 0.01$ ;  $X(\text{V}) \simeq 0.001$ ) are added to the models of each epoch to maintain the concept of a uniform chemical structure despite the slight deterioration of the fitting in the early epochs (i.e., in the outer region of the ejecta). This behavior implies the stratified distribution of these elements.

The best-fit ejecta model contains solely constant chemical mass fractions similar to the abundance structure of the *N5def\_hybrid* model used for the initial input. This simplification allowed us to handle the abundances of the aforementioned elements as free parameters. The synthetic spectra of our best-fit model successfully reproduce all prominent features throughout the studied three week time span (see Fig. 5). Inconsistencies, such as the shift of certain spectral lines, arise due to the simplifications of the fitting method and/or the limitations of the radiative transfer code.

Such mismatches are the shifted synthetic lines that may occur due to the incorrect assumption of constant abundances. The C II  $\lambda 6580$  lines show a consistent redshift compared to the observations, indicating that some level of stratification may be necessary for carbon in the outer layers of the ejecta. Another shortcoming of the synthetic spectra is the lack of several features between 6000 and 8300 Å after maximum, observed as narrow P Cygni lines and previously identified as C II and Fe II features (Tomasella et al. 2016). Since the strong iron features formed close to the photosphere are relatively well reproduced at  $t_{\text{exp}} = 14.8$  and 18.0 days, and both  $X(\text{C})$  and  $X(\text{Fe})$  have constant values throughout the model atmosphere, this issue probably originates from the outer, cooler region of the model ejecta.

The Si and S mass fractions are modified by a few percentage points to improve the fits of the characteristic spectral features  $\lambda 6345$  and  $\lambda 5607$ , respectively. The fractions of two low-

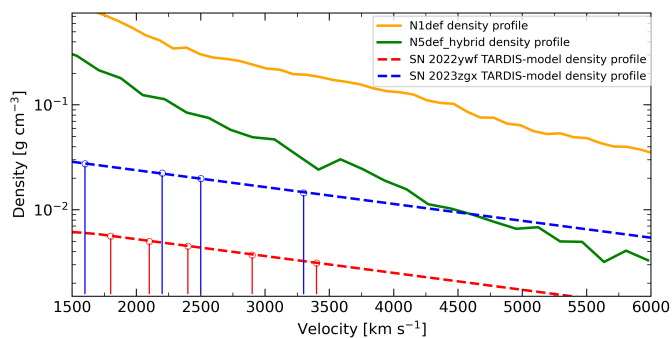


**Fig. 7.** The exponential functions assumed for the density profiles of SNe 2022ywf (red) and 2023zgx (blue) in the best ejecta models, scaled to  $t_{\text{exp}} = 100$  s. The density structures of the two least-luminous pure deflagration models are also plotted for comparison. The vertical lines indicate the location of the photosphere at the fitted epochs in the corresponding models.

abundance elements, Ca and Cr, are changed by factors of  $\sim 3$  to fit the short wavelength end of the spectra as well as the characteristic post-maximum spectral features Cr II  $\lambda 5276$  and the Ca II NIR triplet. However, these discrepancies in the *N5def\_hybrid* hydro model are not significant, as the changes are only up to a few tenths of a percentage point. The main differences arise in IGE abundances, as both the radioactive Ni and the stable Fe are present with significantly lower mass fractions in our model. These updates are required by the fit of the two earliest spectra to reproduce the corresponding lines (see Fig. 5). However, even the reduction of both  $X(\text{Fe})$  and  $X(^{56}\text{Ni})$  mass fractions by  $\sim 0.12$  produces excessively strong Fe III  $\lambda 4420$ ,  $\lambda 5157$ , and Ni II  $\lambda 4068$  lines for the spectrum obtained at  $t_{\text{exp}} = 3.1$  days, but provides a relatively good match for the spectral features at  $t_{\text{exp}} = 5.7$  and 9.8 days. This inconsistency is caused by the use of a uniform chemical structure, as the outer ejecta of SNe Iax may have even lower IGE abundances.

**Table 2.** Physical parameters of the best-fit TARDIS models for SNe 2022ywf and 2023zgx.

	SN 2022ywf	SN 2023zgx
$\rho_0$ [g cm $^{-3}$ ] central density	0.01	0.05
$v_0$ [km s $^{-1}$ ] exponential factor of the density profile	2500	2700
$v_{\text{phot,m}}$ [km s $^{-1}$ ] photospheric velocity at $T_{\text{max}}(r)$	2400	3100
$v_{\text{phot,15}}$ [km s $^{-1}$ ] photospheric velocity at $t_{\text{exp}} = 15$ days	2200	3100

#### 4.2. SN 2023zgx

The spectral series of SN 2023zgx covers a significantly longer period, almost three months of spectral evolution. Although type Iax SNe never go fully nebular, and thus the radiative transfer code assuming a sharp photosphere can be used to reproduce part of the optical regime (Camacho-Neves et al. 2023), the emerg-

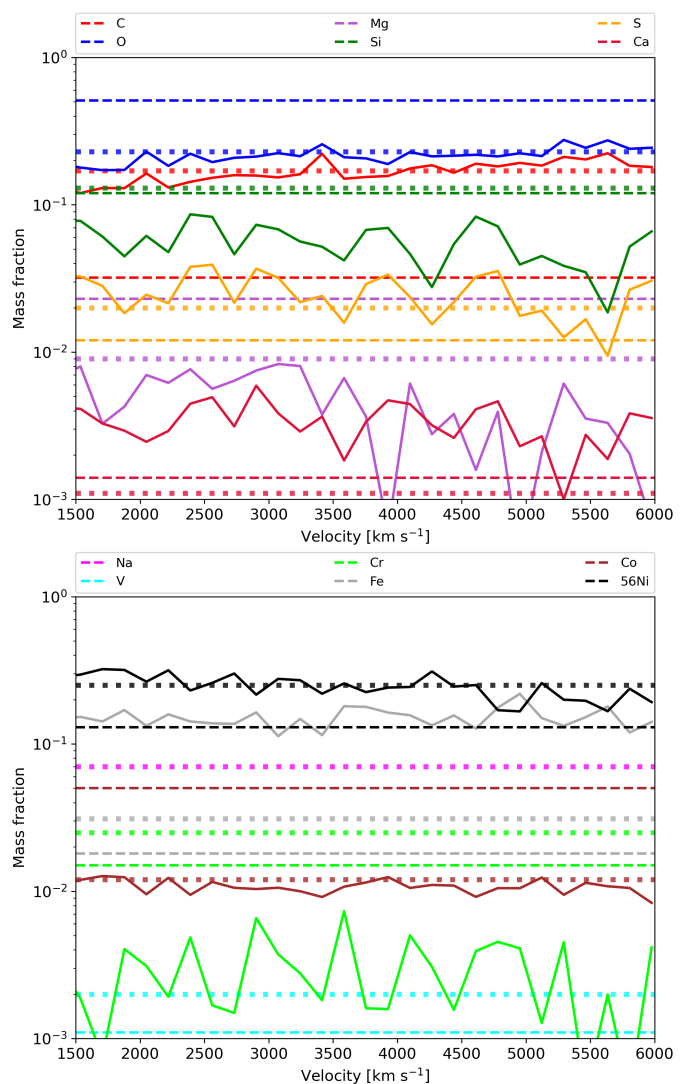


**Fig. 8.** The mass fractions of chemical elements investigated in the abundance tomography analysis of SNe 2022ywf (dashed lines) and 2023zgx (dotted lines). The chemical abundances of the pure deflagration model *N5def\_hybrid* (solid lines) are also shown for comparison. The mass fractions of the radioactive  $^{56}\text{Ni}$  are scaled to  $t_{\text{exp}} = 100$ s.

ing forbidden lines place limitations on the quality of fitting. Because of this, and due to the comparison with the fitting of SN 2022ywf, we fit only the first four epochs (the first five weeks after the explosion, approximately) of the spectral series. The fitting process was repeated with the same principles; however, in contrast to the case of SN 2022ywf, fewer fitting constraints were available due to the lack of early spectra sampling the outermost regions of the ejecta. This circumstance leaves the physical parameters even more uncertain, especially regarding layers over  $5000$  km s $^{-1}$ , which are already at a distance from the photosphere at the first epoch.

By fitting only the post-maximum epochs of SN 2023zgx, its chemical composition is less constrained. This is partially because synthetic spectra, in general, become less sensitive to changes in mass fractions over time. Moreover, the weaker lines cannot be well constrained due to the presence of the strong and overlapping Fe II features. Thus, the distribution of chemical elements that have a significant impact on the pre-maximum spectral features, such as C, S, and Ni, can be effectively described

with the mass fraction obtained from the *N5def\_hybrid* model, which is used as initial input.

Despite the later triggering of follow-up observations, the tomography analysis investigated the same velocity coordinates as those of SN 2022ywf due to its lower expansion velocities. The slope of the inferred ejecta structure of the two SNe is similar, but the layers at the same velocities are denser in the model of SN 2023zgx to reproduce the strong post-maximum IGE features. This may also explain the higher photospheric velocities of SN 2023zgx at the same epochs, regardless of whether they are relative to the maximum or the moment of explosion. This relation also fits into the trend of deflagration models, where more energetic (and luminous) explosions produce more massive ejecta having higher densities, even in the outer regions (Fink et al. 2014; Lach et al. 2022). The angle-averaged density function of *N5def\_hybrid* matches relatively well with that of the best SN 2023zgx model above  $3000 \text{ km s}^{-1}$ , but strongly exceeds it in the deeper ejecta.

The time of the explosion is also more uncertain since  $t_{\text{exp}}$  mainly impacts the spectrum through the dilution of the densities. While the date of the explosion can be narrowed down to approximately  $\pm 1$  day precision in the case of fitting early epochs, the synthetic spectra of SN 2023zgx are relatively insensitive to a change of  $\sim 2$  days in  $t_{\text{exp}}$  due to the lack of pre-maximum spectra. The tomography analysis constrained the date of the explosion to  $T_{\text{exp}} = 60276.1$  MJD, which provides a similar rise time to that of SN 2022ywf.

The synthetic spectra provided by the best-fit model (see Fig. 6) show a good match with the observed ones, as almost all prominent lines are present with the proper optical depth. We also added a high Na abundance to the model ejecta to fit the growing feature around  $5800 \text{ \AA}$ , which has become one of the most prominent P Cygni features at  $t_{\text{exp}} = 33.2$  days, similarly to the late-time spectral synthesis of SNe 2014dt and 2022xlp (Camacho-Neves et al. 2023; Bánhidi et al. 2025, respectively). The only striking difference concerns the NIR triplet of Ca II, where the rising emission of forbidden lines disrupts the fitting based on the photospheric assumptions. Another shortcoming of the fit is that the Fe II lines are too strong between  $4200$  and  $5400 \text{ \AA}$ , resulting from Fe in the outer regions of our model ejecta. The flux continuum is also reproduced for all four spectra, indicating reasonable estimates for the photospheric velocity and the density profile (including  $t_{\text{exp}}$ ). Comparing the fits to those of SN 2022ywf, we can conclude that the spectral evolution of the post-maximum epochs can be better reproduced by the adopted assumptions, indicating a uniform abundance structure for the inner regions of the ejecta.

The constrained ejecta parameters of the best-fit TARDIS models are listed in Tab. 2. The density structures and chemical abundances of SN 2022ywf are shown in Figs. 7 and 8, along with those of SN 2023zgx. We note that our fitting strategy aimed to test the predictions of the corresponding hydrodynamic model *N5def\_hybrid*; thus, the differences between the ejecta models of SNe 2022ywf and 2023zgx are not necessarily real. The constant chemical structure was obtained based on the *N5def\_hybrid* model with modified iron ( $X(\text{Fe}) = 0.025$ ), chromium ( $X(\text{Cr}) = 0.01$ ) and sodium ( $X(\text{Na}) = 0.07$ ) abundances. These changes are mostly consistent with the constrained model atmosphere of SN 2022ywf. Moreover, the abundance structure of SN 2022ywf would result in an indistinguishably good fit for SN 2023zgx as well. This means that those abundances, which differ from the *N5def\_hybrid* model to fit the early spectral features of SN 2022ywf (e.g., decreased carbon

and nickel mass fractions), have no strong impact on spectral formation at post-maximum epochs.

#### 4.3. Comparison with other extremely faint SNe Iax

So far, only five SNe Iax from the faintest end of the luminosity range of the subclass have been published (i.e. with  $M_V < 14$  mag) with detailed follow-up observations before and around maximum light. In this section, we compare the optical spectral evolution and features of SNe 2022ywf and 2023zgx with those of the faint Iax objects, namely SNe 2008ha (Foley et al. 2009), 2020kyg (Singh et al. 2024), 2019gsc (Srivastav et al. 2020; Tomasella et al. 2020) and 2021fcg (Karambelkar et al. 2021).

In Fig. 9, we compare the corresponding spectral epochs before the r-band maximum and approximately 10 days after that. Even though the EL sample shares some common features in their spectral evolution, such as the presence of the Si II  $\lambda 6355$  and the C II  $\lambda 6580$  lines, the strength of these spectral features greatly differs for objects with similar luminosities. These differences are amplified for the post-maximum epoch, when SN 2008ha shows wide absorption of IGEs, while SN 2022ywf represents a more typical set and appearance of P Cygni lines, resembling those of SN 2005hk. SN 2019gsc, on the other hand, lacks strong (pseudo-)emission peaks and shows a significantly slower spectral evolution over 16 days. Since the identified lines are similar, the variation in spectral features may be caused by the different ejecta temperatures. This idea is supported by the color and, thus, the continuum evolution of the objects compared here. While the ejecta temperature of SN 2019gsc barely changes between the epochs in this comparison, SN 2022ywf shifts from a hotter ejecta to a cooler phase, changing the initially presented Fe III and Ni III features to a Fe II dominated post-maximum epoch. The faster cooling of SN 2022ywf can be linked to a steeper density gradient, which is caused by either the different ejecta mass or a line of sight effect, where we have insight to a less dense region of the SN.

The correlation between the peak luminosities and other observables of SNe Iax have been investigated by several studies. Singh et al. (2023) and Magee et al. (2025) presented a correlation between the rise time ( $t_{\text{rise}}$ ) and the peak absolute magnitude in the r-band, as brighter SNe Iax typically reach their maximum later. However, the demonstration of the correlation is still ambiguous due to the limited sample and the high uncertainty of the estimated  $t_{\text{rise}}$  parameters resulting from the relatively late discoveries. The decline parameter  $\Delta m_{15}$ , which shows a greater variance, rather indicates clustering, where the brighter and fainter samples seem to show different behavior (Singh et al. 2023). The lack of strong correlations and the continuous distribution of physical properties throughout the whole luminosity range may indicate that not all transients labeled as type Iax SNe originate from the same explosion scenarios.

Another possible correlation between peak luminosity and expansion velocity has been referred to by multiple studies. Tomasella et al. (2016) investigated a small sample of SNe Iax with spectral coverage around their maximum and constrained  $v_{\text{phot}}$  values. The authors found no proof that SNe Iax with higher velocity also have lower peak absolute magnitudes, as the trend of five objects is spoiled by two outliers, SNe 2009qu (Narayan et al. 2011) and 2014ck (Tomasella et al. 2016), with higher than expected velocities. We note that these statistics are based on sometimes inconsistently estimated  $v_{\text{phot}}$  values. The standard method of calculating the current location of the photosphere, as it is adopted from the analysis of normal SNe Ia, is based

on the blueshift of the absorption feature of the prominent Si II line. Multiple studies (Szalai et al. 2015; Maguire et al. 2023) showed that this method is not reliable for SNe Iax, as the  $\lambda 6355$  feature overlaps with an Fe II absorption comparable even at pre-maximum epochs. Barna et al. (2021) reported a stronger trend between peak luminosity and  $v_{\text{phot}}$  estimated at the moment of B-band maximum light, when the velocities are constrained by abundance tomography. The tomography analysis carried out with a radiative transfer code not only supports the consistency in the comparison of various SNe Iax, but the method also fits the continuum flux and various spectral lines together. This allows us to constrain the bottom of the line forming regions simultaneously and to avoid the incorrect fits due to the misidentification of lines, providing a more certain estimate of  $v_{\text{phot}}$ .

In Fig. 10, the evolution of  $v_{\text{phot}}$  of SNe 2022ywf and 2023zgx are matched with that of other EL SNe Iax. The covered  $v_{\text{phot}}$  curves plotted as a function of  $t_{\text{exp}}$  do not cross each other, which supports the assumption that the relationship between peak luminosity and expansion velocity extends to the extremely low-luminosity range of the subclass as well. For better comparison, we also illustrate the relation of the two physical properties for all SNe Iax with well-studied spectral series in Fig. 11, where the  $v_{\text{phot}}$  values are obtained at the moment of r- (or, if missing, R-)band maximum. We include only those cases where the velocity evolution was mapped by spectral synthesis of radiative transfer codes and had coverage around the maximum light. Assuming monotonically decreasing  $v_{\text{phot}}$  for these epochs, we interpolate to calculate the velocity value for the moment of r- (or, if missing, R-)band maximum. These conditions limit the sample to 13 SNe, which cover almost the entire luminosity range of the subclass, with gaps in the IL group. The seemingly strong correlation between peak luminosities and expansion velocities further supports the assumption that all SNe Iax, including RL, IL, and EL, share a similar origin. Furthermore, the shown trend is not consistent with the scenario of a WD merger resulting in failed detonation, as the simulation predicts relatively high photospheric velocities in the case of an even less luminous SN ( $M_V = -11.3$  mag,  $v_{\text{phot}} = 3900$  km s $^{-1}$  Kashyap et al. 2018). Note that the estimation of  $v_{\text{phot}}$  values in Fig. 11 also required distances and is not fully independent of the constrained luminosities. Thus, the assumed correlation requires further investigation.

## 5. Conclusions

We have presented the photometric and spectroscopic dataset of two SNe Iax from the extremely low-luminosity (EL) regime of the subclass. SN 2022ywf has been the target of the most detailed spectroscopic follow-up from the EL sample so far, including multiple pre-maximum epochs; however, the monitoring ended two weeks after the r-band maximum. The observations of SN 2023zgx started only after its peak, but the follow-up covers  $\sim 100$  days. In this study, we mainly focused on the first month after the explosions, when the photospheric assumption is relatively robust for SNe Iax, and the observations of the two objects overlap.

The comparison of the spectroscopic datasets showed that the first three epochs of SN 2023zgx (between +1.4 and +7.1 days) almost perfectly fit the spectra of SN 2022ywf. However, the corresponding epochs indicate a slightly faster evolution for SN 2022ywf, which may be linked to the steeper density gradient of the ejecta. Similar conclusions can be drawn from the comparison of other EL SNe Iax with similar spectral epochs.

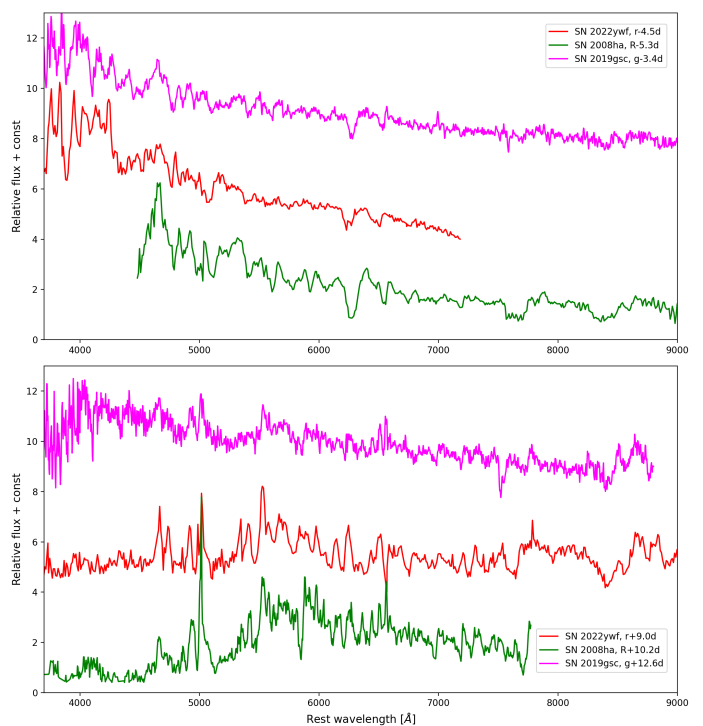


**Fig. 9.** Spectral comparison at similar epochs between three SNe Iax from the EL sample. The spectra are corrected for reddening and redshift; epochs are taken from the corresponding publications of SNe 2008ha (Foley et al. 2009; Valenti et al. 2009) and 2019gsc (Srivastav et al. 2020).

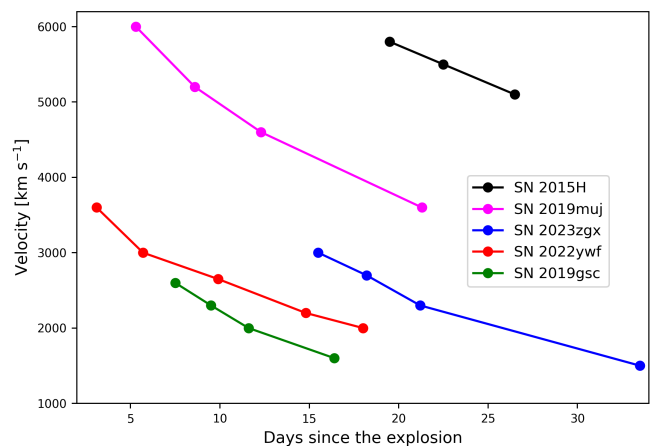


**Fig. 10.** Photospheric velocity evolution of EL and IL SNe Iax constrained by abundance tomography method.

The spectroscopic time series of SNe 2022ywf and 2023zgx were studied by the abundance tomography method, which allowed us to map the ejecta properties of both objects.

1. The comparison of the observables with other objects of the EL sample revealed differences in the post-maximum LC and color evolution.
2. The density structures inferred from the abundance tomography analysis of SNe 2022ywf and 2023zgx are comparable to those of the *N5def\_hybrid* model and, thus, to each other. Considering that both SNe have lower peak luminosities than the pure deflagration model, the lower densities are consistent with expectations.

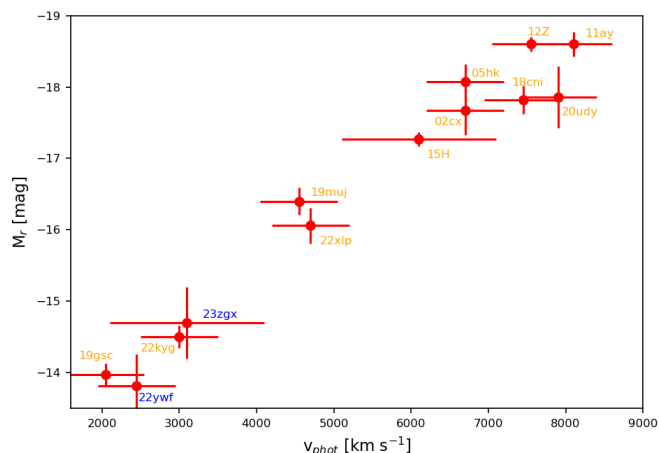


**Fig. 11.** Absolute magnitudes in r/R-band of SNe Ia as a function of their photospheric velocity at the moment of maximum light. We only plot those SNe Ia which have been the subject of abundance tomography. In case of no spectral coverage of the maximum (SNe 2015H and 2023zgx), photospheric velocity is estimated with linear extrapolation. The corresponding references are listed in Tab. A.7.

3. The derived uniform abundance models are also consistent with the predictions of the deflagration models but show slightly lower IGE mass fractions.
4. The photospheric evolution of the two studied SNe fits into the general trend of type Ia SNe, as the more luminous objects tend to show higher velocities at the same epochs.

The analysis of SNe 2022ywf and 2023zgx revealed that the evolution of the extremely low-luminosity objects can be efficiently described by the general properties of the pure deflagration models, such as the constant chemical abundances and a steep density profile. These results support the assumption that, despite the diversity in observables, the EL Ia SNe share the same origin. In the wider context, the intrinsic similarities can be extended to all SNe Ia. We showed that the correlation between peak absolute magnitudes and expansion velocities at the time of maximum light may extend to the extremely low-luminosity group. The continuous distribution of certain physical properties through the luminosity range of the subclass makes it probable that all SNe Ia originate from similar explosion scenarios.

**Acknowledgements.** This work uses data from the Las Cumbres Observatory Global Telescope network. The LCO team is supported by NSF grants AST-2308113 and AST-1911151. Based on observations collected at the European Organisation for Astronomical Research in the Southern Hemisphere, Chile, as part of ePESSTO+ (the advanced Public ESO Spectroscopic Survey for Transient Objects Survey – PI: Inserra). ePESSTO+ observations were obtained under ESO program IDs 108.220C and 112.25JQ. This project has received funding from the HUN-REN Hungarian Research Network. B.B. received support from the Hungarian National Research, Development and Innovation Office grants OTKA PD-147091. T.-W.C. acknowledges the financial support from the Yushan Fellow Program by the Ministry of Education, Taiwan (MOE-111-YSFMS-0008-001-P1) and the National Science and Technology Council, Taiwan (NSTC grant 114-2112-M-008-021-MY3). T.E.M.B. is funded by Horizon Europe ERC grant no. 101125877. Time-domain research by the University of Arizona team and D.J.S. is supported by National Science Foundation (NSF) grants 2108032, 2308181, 2407566, and 2432036 and the Heising-Simons Foundation under grant #2020-1864. TP acknowledges the financial support from the Slovenian Research Agency (grants I0-0033, P1-0031, J1-8136, J1-2460 and Z1-1853). KAB is supported by an LSST-DA Catalyst Fellowship; this publication was thus made possible through the support of Grant 62192 from the John Templeton Foundation to LSST-DA. Supernova research at Rutgers University is supported in part by NSF grant AST-2407567. SWJ also gratefully acknowledges support from a Guggenheim Fellowship. KAB is supported by an LSST-DA Catalyst Fellowship; this publication was thus made possible through the support of Grant 62192 from the John Templeton Foundation to LSST-DA.

## References

- Bánhidí, D., Barna, B., Szalai, T., et al. 2025, *A&A*, 703, A64
- Barna, B., Szalai, T., Jha, S. W., et al. 2021, *MNRAS*, 501, 1078
- Barna, B., Szalai, T., Kerzendorf, W. E., et al. 2018, *MNRAS*, 480, 3609
- Barna, B., Szalai, T., Kromer, M., et al. 2017, *MNRAS*, 471, 4865
- Bostroem, K. A., Valenti, S., Sand, D. J., et al. 2022, *Transient Name Server Classification Report*, 2022-3154, 1
- Brown, T. M., Baliber, N., Bianco, F. B., et al. 2013, *PASP*, 125, 1031
- Buzzoni, B., Delabre, B., Dekker, H., et al. 1984, *Msngr*, 38, 9
- Camacho-Neves, Y., Jha, S. W., Barna, B., et al. 2023, *ApJ*, 951, 67
- Chonis, T. S., Hill, G. J., Lee, H., Tuttle, S. E., & Vattiat, B. L. 2014, in *Ground-Based and Airborne Instrumentation for Astronomy V*, Vol. 9147 (International Society for Optics and Photonics), 91470A
- Clemens, J. C., Crain, J. A., & Anderson, R. 2004, in *Society of Photo-Optical Instrumentation Engineers (SPIE) Conference Series*, Vol. 5492, *Ground-based Instrumentation for Astronomy*, ed. A. F. M. Moorwood & M. Iye, 331–340
- Crimes, A., Levan, A., Leloudas, G., et al. 2023, *Transient Name Server Classification Report*, 2023-3247, 1
- Dimitriadis, G., Burgaz, U., Deckers, M., et al. 2025, *A&A*, 694, A10
- Fink, M., Kromer, M., Seitenzahl, I. R., et al. 2014, *MNRAS*, 438, 1762
- Firth, R. E., Sullivan, M., Gal-Yam, A., et al. 2015, *MNRAS*, 446, 3895
- Foley, R. J., Challis, P. J., Chornock, R., et al. 2013, *ApJ*, 767, 57
- Foley, R. J., Chornock, R., Filippenko, A. V., et al. 2009, *AJ*, 138, 376
- Hook, I. M., Jørgensen, I., Allington-Smith, J. R., et al. 2004, *PASP*, 116, 425
- Jordan, IV, G. C., Perets, H. B., Fisher, R. T., & van Rossum, D. R. 2012, *ApJ*, 761, L23
- Karambelkar, V. R., Kasliwal, M. M., Maguire, K., et al. 2021, *ApJ*, 921, L6
- Kashyap, R., Haque, T., Lorén-Aguilar, P., García-Berro, E., & Fisher, R. 2018, *ApJ*, 869, 140
- Kerzendorf, W. E. & Sim, S. A. 2014, *MNRAS*, 440, 387
- Kromer, M., Fink, M., Stanishev, V., et al. 2013, *MNRAS*, 429, 2287
- Kromer, M., Ohlmann, S. T., Pakmor, R., et al. 2015, *MNRAS*, 450, 3045
- Kwok, L. A., Singh, M., Jha, S. W., et al. 2025, *ApJ*, 989, L33
- Lach, F., Callan, F. P., Bubeck, D., et al. 2022, *A&A*, 658, A179
- Leung, S.-C. & Nomoto, K. 2020, *ApJ*, 900, 54
- Li, W., Filippenko, A. V., Chornock, R., et al. 2003, *PASP*, 115, 453
- Long, M., Jordan, IV, G. C., van Rossum, D. R., et al. 2014, *ApJ*, 789, 103
- Magee, M. R., Killestein, T. L., Pursiainen, M., et al. 2025, *arXiv e-prints*, arXiv:2506.02118
- Magee, M. R., Kotak, R., Sim, S. A., et al. 2016, *A&A*, 589, A89
- Magee, M. R., Maguire, K., Kotak, R., et al. 2020, *A&A*, 634, A37
- Maguire, K., Magee, M. R., Leloudas, G., et al. 2023, *MNRAS*, 525, 1210
- McCully, C., Jha, S. W., Foley, R. J., et al. 2014, *Nature*, 512, 54
- Narayan, G., Foley, R. J., Berger, E., et al. 2011, *ApJ*, 731, L11
- Phillips, M. M. 1993, *ApJ*, 413, L105
- Piro, A. L. & Nakar, E. 2013, *ApJ*, 769, 67
- Ramsey, L. W., Adams, M. T., Barnes, T. G., et al. 1998, in *Society of Photo-Optical Instrumentation Engineers (SPIE) Conference Series*, Vol. 3352, *Advanced Technology Optical/IR Telescopes VI*, ed. L. M. Stepp, 34–42
- Riess, A. G., Filippenko, A. V., Li, W., et al. 1999, *AJ*, 118, 2675
- Shingles, L., Smith, K. W., Young, D. R., et al. 2021, *Transient Name Server AstroNote*, 7, 1
- Singh, M., Kwok, L. A., Jha, S. W., et al. 2025, *arXiv e-prints*, arXiv:2505.02943
- Singh, M., Sahu, D. K., Barna, B., et al. 2024, *ApJ*, 965, 73
- Singh, M., Sahu, D. K., Dastidar, R., et al. 2023, *ApJ*, 953, 93
- Smartt, S. J., Valenti, S., Fraser, M., et al. 2015, *A&A*, 579, A40
- Srivastav, S., Smartt, S. J., Huber, M. E., et al. 2022a, *MNRAS*, 511, 2708
- Srivastav, S., Smartt, S. J., Huber, M. E., et al. 2023, *ApJ*, 943, L20
- Srivastav, S., Smartt, S. J., Leloudas, G., et al. 2020, *ApJ*, 892, L24
- Srivastav, S., Smith, K. W., Young, D. R., et al. 2022b, *Transient Name Server AstroNote*, 234, 1
- Stritzinger, M. D., Valenti, S., Hoefflich, P., et al. 2015, *A&A*, 573, A2
- Szalai, T., Vinkó, J., Sárneczky, K., et al. 2015, *MNRAS*, 453, 2103
- Taubenberger, S. 2017, in *Handbook of Supernovae*, ed. A. W. Alsabti & P. Murdin, 317
- Tomasella, L., Cappellaro, E., Benetti, S., et al. 2016, *MNRAS*, 459, 1018
- Tomasella, L., Stritzinger, M., Benetti, S., et al. 2020, *MNRAS*, 496, 1132
- Tonry, J. L., Denneau, L., Heinze, A. N., et al. 2018, *PASP*, 130, 064505
- Tully, R. B., Courtois, H. M., & Sorce, J. G. 2016, *AJ*, 152, 50
- Tully, R. B. & Fisher, J. R. 1988, *Catalog of Nearby Galaxies*
- Valenti, S., Pastorello, A., Cappellaro, E., et al. 2009, *Nature*, 459, 674

## Appendix A: Some extra material

Table A.1. Log of ATLAS photometry of SN 2022ywf.

MJD	Filter	Flux	mag
59875.18	c	9.0 (5.97)	>20.77
59876.42	c	2.6 (6.34)	>20.70
59876.95	o	31.1 (11.8)	>20.03
59878.41	o	3.21 (6.34)	>20.70
59879.19	c	10.9 (6.34)	>20.70
59880.45	c	52.7 (6.71)	19.60 (0.14)
59880.77	o	56.2 (11.76)	19.53 (0.23)
59882.41	o	114.1 (5.97)	18.76 (0.06)
59883.16	o	140.5 (5.87)	18.53 (0.05)
59884.41	o	164.1 (6.84)	18.36 (0.05)
59884.90	o	156.9 (23.1)	18.41 (0.16)
59886.36	o	149.0 (7.88)	18.47 (0.06)
59887.11	o	174.3 (13.4)	18.30 (0.08)
59892.48	o	202.4 (15.2)	18.13 (0.08)
59892.92	o	171.2 (17.8)	18.32 (0.11)
59894.38	o	176.0 (8.2)	18.29 (0.05)
59896.45	o	172.3 (9.2)	18.31 (0.06)
59896.88	c	103.4 (5.7)	18.86 (0.06)
59898.39	c	120.0 (3.8)	18.70 (0.04)
59899.12	o	148.0 (7.0)	18.47 (0.05)
59900.49	o	141.4 (13.7)	18.52 (0.11)
59900.86	c	82.4 (7.2)	19.11 (0.10)
59902.30	c	57.5 (3.2)	19.50 (0.06)
59903.11	o	118.8 (6.6)	18.71 (0.06)
59906.34	c	65.7 (4.6)	19.36 (0.08)
59907.10	o	114.9 (9.5)	18.75 (0.09)
59908.35	o	91.5 (7.6)	19.00 (0.09)
59908.97	c	61.8 (7.0)	19.42 (0.12)
59911.09	o	83.7 (8.3)	19.09 (0.11)
59912.84	o	65.6 (7.3)	19.36 (0.12)
59915.05	o	77.4 (15.0)	19.18 (0.21)
59923.11	o	46.6 (9.8)	19.73 (0.23)
59927.09	c	25.0 (4.7)	20.41 (0.21)
59928.31	c	32.2 (5.4)	20.13 (0.18)
59931.06	c	29.8 (5.3)	20.22 (0.19)

**Table A.2.** Log of ATLAS photometry of SN 2023zgx

MJD	Filter	Flux	mag
60294.63	o	351.3 (8.4)	17.53 (0.02)
60296.61	c	230.4 (10.3)	17.99 (0.04)
60299.34	o	290.0 (10.6)	17.74 (0.04)
60301.07	o	244.6 (9.03)	17.92 (0.04)
60304.63	o	188.1 (10.3)	18.21 (0.05)
60306.57	o	184.2 (11.0)	18.23 (0.06)
60308.59	o	164.6 (9.9)	18.35 (0.06)
60309.54	o	149.3 (12.0)	18.46 (0.08)
60310.50	o	132.2 (17.1)	18.59 (0.14)
60314.61	o	127.9 (7.5)	18.63 (0.06)
60324.59	o	97.6 (6.4)	18.92 (0.07)
60327.35	o	78.2 (9.6)	19.16 (0.13)
60329.02	c	58.0 (5.9)	19.49 (0.11)
60331.33	o	94.9 (6.4)	18.95 (0.07)
60333.04	o	66.0 (12.9)	19.35 (0.21)
60336.51	o	71.3 (12.6)	19.26 (0.19)
60344.50	c	37.7 (6.2)	19.96 (0.18)
60347.33	o	64.1 (7.7)	19.38 (0.13)
60348.55	c	40.9 (5.5)	19.87 (0.14)
60349.04	o	66.4 (6.7)	19.34 (0.11)
60350.48	o	61.4 (6.0)	19.43 (0.10)
60351.18	o	66.5 (7.1)	19.34 (0.11)
60353.06	o	55.0 (6.1)	19.54 (0.12)
60355.26	o	50.6 (6.3)	19.63 (0.13)
60356.95	o	55.6 (8.1)	19.53 (0.16)
60361.03	o	47.4 (6.4)	19.71 (0.14)

**Table A.3.** Log of SN 2022ywf *BVgri* photometry.

MJD	B	V	g	r	i	Observatory
59880.84	19.05 (0.05)	19.80 (0.16)	19.15 (0.04)	19.50 (0.10)	19.51 (0.14)	LCO
59881.86	18.61 (0.04)	18.91 (0.07)	18.70 (0.03)	18.77 (0.06)	19.02 (0.10)	LCO
59885.15	18.21 (0.03)	18.32 (0.03)	18.17 (0.01)	18.28 (0.02)	18.50 (0.03)	LCO
59886.25	18.17 (0.03)	18.30 (0.03)	18.14 (0.02)	18.24 (0.02)	18.50 (0.04)	LCO
59887.99	18.40 (0.05)	18.32 (0.05)	18.33 (0.09)	18.25 (0.05)	18.43 (0.06)	LCO
59891.80	- (-)	- (-)	- (-)	18.14 (0.16)	18.10 (0.11)	LCO
59892.50	- (-)	18.47 (0.07)	18.63 (0.05)	18.15 (0.06)	18.15 (0.07)	LCO
59893.80	18.95 (0.09)	18.62 (0.12)	18.80 (0.06)	18.14 (0.05)	18.28 (0.08)	LCO
59900.12	19.80 (0.05)	19.35 (0.05)	19.60 (0.04)	18.44 (0.03)	18.51 (0.05)	LCO
59903.18	20.11 (0.06)	19.51 (0.06)	19.91 (0.04)	18.80 (0.03)	18.70 (0.04)	LCO
59906.17	20.03 (0.06)	19.49 (0.05)	20.09 (0.04)	19.05 (0.03)	18.69 (0.05)	LCO
59908.49	20.43 (0.08)	19.66 (0.06)	20.12 (0.04)	19.16 (0.03)	19.01 (0.04)	LCO
59919.12	20.74 (0.38)	20.11 (0.33)	20.40 (0.30)	19.38 (0.14)	19.83 (0.27)	LCO
59923.13	20.35 (0.15)	20.02 (0.16)	20.55 (0.18)	19.71 (0.11)	19.88(0.16)	LCO
59927.05	20.18 (0.08)	- (-)	20.29 (0.07)	- (-)	19.67 (0.09)	LCO
59931.07	20.69 (0.08)	20.97 (0.17)	20.93 (0.09)	20.05 (0.05)	20.05 (0.12)	LCO
59936.90	21.02 (0.12)	20.93 (0.19)	20.79 (0.09)	20.37 (0.11)	20.03 (0.09)	LCO
59937.95	- (-)	- (-)	20.97 (0.18)	20.07 (0.12)	20.27 (0.25)	LCO
59960.45	- (-)	- (-)	21.32 (0.17)	20.22 (0.08)	19.97 (0.13)	LCO
59973.12	- (-)	- (-)	- (-)	21.02 (0.54)	20.14 (0.23)	LCO
59984.09	- (-)	- (-)	21.51 (0.17)	20.65 (0.13)	20.34 (0.14)	LCO

**Table A.4.** Log of the spectra of SN 2022ywf.

Date	MJD	$t_{\text{exp}}$ [d]	Phase [d]	Telescope/Instrument	Wavelength range [Å]
2022-10-29	59881.3	2.9	-9.1	APO/Kosmos	3500 - 6500
2022-10-29	59881.5	3.1	-8.9	LCO/FLOYDS	3500 - 10000
2022-10-31	59883.8	5.4	-6.6	SALT/RSS	3500 - 7250
2022-11-01	59884.1	5.7	-6.3	SOAR/GHTS_RED	3700 - 7050
2022-11-02	59885.9	7.5	-4.5	SALT/RSS	3500 - 7250
2022-11-04	59887.1	8.7	-3.3	SOAR/GHTS_RED	5000 - 9000
2022-11-05	59888.2	9.8	-2.2	HET/LRS	3650 - 10000
2022-11-08	59891.8	13.4	+1.4	SALT/RSS	3500 - 7250
2022-11-09	59892.8	14.4	+2.4	SALT/RSS	3500 - 7250
2025-11-10	59893.2	14.8	+2.8	HET/LRS	3700 - 10000
2025-11-10	59894.0	15.6	+3.6	LT/SPRAT	4050 - 8000
2025-11-12	59895.2	16.8	+4.8	HET/LRS	3700 - 6900
2025-11-13	59896.3	17.9	+5.9	HET/LRS	6400 - 10000
2022-11-13	59896.4	18.0	+6.0	LCO/FLOYDS	3500 - 10000
2025-11-13	59897.0	18.6	+6.6	LT/SPRAT	4050 - 8000
2022-11-16	59899.2	20.8	+8.8	Bok/B&C	4000 - 8000
2022-11-16	59899.3	20.9	+8.9	NTT/EFOSC2	3800 - 9300
2022-11-16	59899.4	21.0	+9.0	LCO/FLOYDS	3500 - 10000

**Notes.**  $t_{\text{exp}}$  shows the time since the date of explosion constrained in the abundance tomography (MJD 59878.4); while the phases are given relative to the maximum in r-band (MJD 59890.4).

**Table A.5.** Log of LCO photometry of SN 2023zgx

MJD	B	V	g	r	i	z	Observatory
60294.12	18.95 (0.26)	17.90 (0.10)	18.11 (0.11)	17.48 (0.09)	17.47 (0.09)	17.33 (0.15)	RC80
60294.15	18.75 (0.20)	17.70 (0.12)	18.16 (0.12)	17.40 (0.12)	17.35 (0.10)	17.07 (0.16)	BRC80
60294.73	18.95 (0.06)	17.81 (0.03)	- (-)	- (-)	- (-)	- (-)	LCO
60296.13	19.07 (0.31)	18.14 (0.13)	18.33 (0.16)	17.71 (0.10)	17.61 (0.12)	17.37 (0.24)	RC80
60296.17	19.00 (0.25)	17.69 (0.18)	18.20 (0.16)	17.58 (0.12)	17.51 (0.10)	17.42 (0.19)	BRC80
60296.35	19.13 (0.07)	17.94 (0.03)	18.42 (0.02)	17.66 (0.02)	17.61 (0.02)	- (-)	LCO
60297.11	19.37 (0.29)	18.20 (0.11)	18.54 (0.14)	17.85 (0.11)	17.77 (0.12)	17.52 (0.14)	RC80
60298.13	19.49 (0.27)	18.13 (0.10)	18.36 (0.12)	17.83 (0.08)	17.75 (0.09)	17.42 (0.15)	RC80
60298.33	19.18 (0.07)	18.06 (0.04)	18.50 (0.03)	17.81 (0.02)	17.69 (0.03)	- (-)	LCO
60300.09	19.03 (0.37)	18.02 (0.09)	18.77 (0.10)	17.90 (0.07)	- (-)	- (-)	LCO
60304.35	19.12 (0.36)	18.33 (0.29)	18.80 (0.10)	18.17 (0.06)	17.88 (0.11)	- (-)	LCO
60305.44	19.86 (0.60)	18.68 (0.19)	18.64 (0.12)	18.20 (0.09)	18.21 (0.08)	- (-)	LCO
60307.07	19.55 (0.23)	18.52 (0.11)	19.04 (0.10)	18.37 (0.06)	18.29 (0.07)	- (-)	BRC80
60308.20	20.04 (0.28)	18.81 (0.12)	19.16 (0.08)	18.36 (0.06)	18.35 (0.07)	- (-)	LCO
60309.07	- (-)	18.87 (0.30)	19.08 (0.27)	18.56 (0.12)	18.36 (0.12)	17.89 (0.17)	RC80
60309.25	19.83 (0.17)	18.54 (0.08)	18.81 (0.05)	18.33 (0.05)	18.20 (0.06)	- (-)	LCO
60310.43	19.80 (0.17)	18.74 (0.09)	19.48 (0.13)	18.42 (0.06)	18.32 (0.08)	- (-)	LCO
60315.51	20.41 (0.18)	18.93 (0.05)	19.33 (0.05)	18.76 (0.04)	18.52 (0.04)	- (-)	LCO
60319.04	- (-)	19.20 (0.19)	19.52 (0.17)	18.78 (0.14)	18.70 (0.19)	- (-)	RC80
60320.05	- (-)	19.13 (0.16)	19.76 (0.21)	19.02 (0.12)	- (-)	- (-)	RC80
60322.05	- (-)	- (-)	- (-)	18.94 (0.21)	18.62 (0.22)	- (-)	RC80
60322.68	20.40 (0.12)	19.28 (0.06)	19.64 (0.07)	19.42 (0.25)	18.60 (0.05)	- (-)	LCO
60326.04	- (-)	19.24 (0.23)	19.81 (0.28)	- (-)	18.65 (0.18)	- (-)	RC80
60328.35	20.52 (0.06)	19.35 (0.04)	19.80 (0.04)	19.13 (0.03)	18.79 (0.03)	- (-)	LCO
60329.04	- (-)	19.04 (0.37)	- (-)	19.00 (0.20)	- (-)	18.20 (0.34)	RC80
60330.02	- (-)	- (-)	- (-)	19.13 (0.26)	19.05 (0.28)	- (-)	RC80
60331.09	- (-)	19.16 (0.33)	19.41 (0.37)	19.13 (0.20)	18.69 (0.17)	18.82 (0.36)	RC80
60332.32	20.59 (0.13)	19.45 (0.06)	19.93 (0.06)	19.27 (0.05)	18.84 (0.03)	- (-)	LCO
60333.08	- (-)	- (-)	19.45 (0.38)	19.13 (0.17)	- (-)	- (-)	RC80
60335.02	- (-)	19.37 (0.25)	- (-)	- (-)	18.75 (0.26)	- (-)	RC80
60336.15	20.71 (0.42)	19.38 (0.16)	20.10 (0.21)	19.28 (0.12)	19.05 (0.11)	- (-)	LCO
60338.09	- (-)	- (-)	20.38 (0.61)	19.27 (0.16)	18.62 (0.14)	- (-)	BRC80
60342.29	21.07 (0.26)	19.76 (0.11)	20.10 (0.11)	19.32 (0.06)	18.96 (0.06)	- (-)	LCO
60346.11	20.40 (0.21)	19.72 (0.12)	19.81 (0.09)	18.99 (0.05)	19.06 (0.08)	18.93 (0.20)	BRC80
60347.22	20.92 (0.11)	19.76 (0.06)	20.27 (0.06)	19.52 (0.04)	19.09 (0.04)	- (-)	LCO

60350.93	21.03 (0.23)	20.19 (0.14)	20.33 (0.08)	19.70 (0.07)	19.07 (0.08)	- (-)	LCO
60355.09	21.38 (0.32)	19.96 (0.11)	20.58 (0.09)	19.77 (0.08)	19.54 (0.10)	- (-)	LCO
60357.02	- (-)	20.01 (0.19)	20.23 (0.15)	19.69 (0.11)	19.30 (0.10)	18.52 - (-)	BRC80
60359.11	21.51 (0.24)	20.39 (0.13)	20.66 (0.10)	19.98 (0.08)	19.26 (0.08)	- (-)	LCO
60362.94	20.61 (0.41)	20.00 (0.24)	20.01 (0.20)	20.21 (0.37)	19.35 (0.18)	- (-)	LCO
60369.97	21.34 (0.64)	20.34 (0.33)	20.38 (0.26)	19.95 (0.21)	19.27 (0.12)	- (-)	LCO
60374.26	21.14 (0.24)	21.11 (0.29)	20.83 (0.13)	20.22 (0.08)	19.51 (0.06)	- (-)	LCO
60378.18	21.94 (0.27)	20.52 (0.12)	20.95 (0.12)	20.23 (0.08)	19.54 (0.06)	- (-)	LCO
60382.13	21.79 (0.31)	20.80 (0.20)	21.44 (0.25)	20.43 (0.15)	19.67 (0.13)	- (-)	LCO
60387.84	22.22 (0.91)	20.77 (0.45)	21.61 (0.48)	20.56 (0.14)	19.71 (0.08)	- (-)	LCO
60389.03	- (-)	20.55 (0.48)	20.93 (0.47)	19.88 (0.17)	19.56 (0.17)	- (-)	BRC80
60392.09	- (-)	20.48 (1.09)	19.75 (0.60)	20.36 (0.22)	19.10 (0.15)	- (-)	LCO
60397.25	23.16 (2.07)	20.98 (0.45)	- (-)	- (-)	- (-)	- (-)	LCO
60404.90	22.48 (0.52)	21.05 (0.21)	21.93 (0.32)	21.05 (0.25)	20.00 (0.16)	- (-)	LCO
60416.92	23.76 (2.19)	21.84 (0.56)	22.70 (0.79)	21.75 (0.48)	20.88 (0.29)	- (-)	LCO
60424.80	- (-)	- (-)	21.60 (1.65)	20.95 (0.82)	20.21 (0.43)	- (-)	LCO
60432.97	23.50 (1.02)	22.76 (0.80)	- (-)	- (-)	- (-)	- (-)	LCO
60440.98	- (-)	22.25 (0.65)	- (-)	- (-)	- (-)	- (-)	LCO
60451.80	- (-)	- (-)	21.22 (1.07)	20.56 (0.50)	20.12 (0.36)	- (-)	LCO

Table A.6. Log of the spectra of SN 2023zgx

Date	MJD	$t_{\text{exp}}$ [d]	Phase [d]	Telescope/Instrument	Wavelength range [Å]
2023-12-13	60291.6	15.5	+1.2	Gemini-N/GMOS	4700 - 9250
2023-12-16	60294.3	18.2	+3.9	NTT/EFOSC2	3650 - 9220
2023-12-19	60297.3	21.2	+6.9	NTT/EFOSC2	3650 - 9220
2023-12-31	60309.3	33.2	+18.9	NTT/EFOSC2	3650 - 9220
2024-01-06	60315.6	39.5	+25.2	LCO/FLOYDS	3500-10000
2024-01-13	60322.7	46.6	+32.3	LCO/FLOYDS	3500-10000
2024-01-16	60325.3	49.2	+34.9	NTT/EFOSC2	3650 - 9220
2024-02-04	60344.6	68.5	+54.2	LCO/FLOYDS	3500 - 10000
2024-02-12	60352.5	76.4	+62.1	LCO/FLOYDS	3500 - 10000
2024-02-20	60360.6	84.5	+70.2	LCO/FLOYDS	3500 - 10000
2024-03-01	60370.9	94.8	+80.5	SALT/RSS	3500 - 7250
2024-03-02	60371.9	95.8	+81.5	SALT/RSS	3500 - 7250
2024-03-10	60379.0	103.9	+89.6	SALT/RSS	3500 - 7250
2024-03-11	60380.0	104.9	+90.6	SALT/RSS	3500 - 7250

**Notes.**  $t_{\text{exp}}$  shows the time since the date of explosion constrained in the abundance tomography (MJD 60276.1); while the phases are given relative to the maximum in r-band (MJD 60290.4).

Table A.7. The peak absolute magnitudes in r/R-band and photospheric velocities of type Ia SNe at the moment of maximum light.

Supernova	$M_r$		$v_{\text{phot}}$	
SN 2011ay	-18.60	Szalai et al. (2015)	8100	Barna et al. (2017)
SN 2012Z	-18.60	Stritzinger et al. (2015)	7600	Barna et al. (2018)
SN 2005hk	-18.07	Stritzinger et al. (2015)	6700	Barna et al. (2018)
SN 2020udy	-17.86	Maguire et al. (2023)	7900	Singh et al. (2024)
SN 2018cni	-17.82	Singh et al. (2023)	7500	Singh et al. (2023)
SN 2002cx	-17.67	Li et al. (2003)	6700	Barna et al. (2018)
SN 2015H	-17.27	Magee et al. (2016)	6100	Barna et al. (2018)
SN 2019muj	-16.40	Barna et al. (2021)	4600	Barna et al. (2021)
SN 2022xlp	-16.06	Bánhidi et al. (2025)	4700	Bánhidi et al. (2025)
SN 2023zgx	-14.70	This work	3100	This work
SN 2020kyg	-14.50	Singh et al. (2023)	3000	Singh et al. (2023)
SN 2019gsc	-13.97	Srivastav et al. (2020)	2100	Srivastav et al. (2020)
SN 2022ywf	-13.81	This work	2400	This work